Published in final edited form as:
Clin Cancer Res. 2019 December 15; 25(24): 7436–7447. doi:10.1158/1078-0432.CCR-19-0360.

Longitudinal photoacoustic imaging of the pharmacodynamic effect of vascular targeted therapy on tumors

S. Peter Johnson[#1], **Olumide Ogunlade**[#2], **Mark F. Lythgoe**[3], **Paul Beard**[2], **R. Barbara Pedley**[1]

[1]UCL Cancer Institute, University College London, Gower Street, London, WC1E 6BT

[2]UCL Department of Medical Physics and Biomedical Engineering, University College London, Gower Street, London, WC1E 6BT

[3]UCL Centre for Advanced Biomedical Imaging, Division of Medicine, University College London, Gower Street, London, WC1E 6BT

[#] These authors contributed equally to this work.

Abstract

Purpose—Photoacoustic imaging (PAI) is a novel non-invasive non-ionising imaging technique that allows longitudinal imaging of tumor vasculature *in vivo* and monitoring of response to therapy, especially for vascular targeted chemotherapy agents. In this study we used a novel high resolution all optical PAI scanner to observe the pharmacodynamic response to the vascular disrupting agent OXi4503.

Experimental Design—two models of colorectal carcinoma (SW1222 and LS174T) that possess differing pathophysiological vascularisation were established as subcutaneous tumors in mice. Monitoring of response was performed over a 16-day 'regrowth' period following treatment at 40mg/kg, and at day 2 for a 'dose response' study at 40mg/kg, 10mg/kg, 1mg/kg and sham dose.

Results—qualitative and quantitative changes in PA signal are observed, with an initial decrease followed by a plateau and subsequent return of signal indicating regrowth. Both tumor types exhibited a decrease in signal however the more vascularised SW1222 tumors show greater response to treatment. Decreasing the dose of OXi4503 led to a decrease in PA signal intensity of 60%, 52% and 20% in SW1222 tumors and 30%, 26% and 4% for LS174T tumors.

Conclusion—we have shown for the first time that PAI can observe the pharmacodynamic response of tumor vasculature to drug treatment both longitudinally and at different dose levels. Assessment of differing response to treatment based on vascular pathophysiological differences

Correspondence to: S. Peter Johnson.

Corresponding author: Dr Sean Peter Johnson, The Francis Crick Institute, 1 Midland Road, London, NW1 1AT, UK, Tel. + 00 44 203 796 2745, peter.johnson@crick.ac.uk.

Additional information: This work was also supported by King's College London and University College London Comprehensive Cancer Imaging Centre, Cancer Research UK and the Engineering and Physical Sciences Research Council (EPSRC), in association with the Medical Research Council and Department of Health, UK (C1519/A10331) and ERC Advanced Grant Ref: 741149

P. Beard has a financial interest in DeepColor SAS. However, DeepColor SAS had no involvement in this work. The other authors declare no potential conflicts of interest

Europe PMC Funders Author Manuscripts

between patients has the potential to provide personalised drug therapy; we have demonstrated that PAI, which is clinically translatable, could be a powerful tool for this purpose.

Keywords

Photoacoustic; preclinical; tumor; OXi4503; Pharmacodynamic

Europe PMC Funders Author Manuscripts

Introduction

The development of novel therapeutics for the treatment of cancer is an attritional process, with only ≈5% of lead compounds that enter clinical trials becoming regulatory approved therapies [1]. A better understanding of the effect of drug action on the specific microenvironment target would greatly increase the translational relevance of preclinical studies, and therefore increase drug approval, which would save time and resources [2, 3]. The use of biomedical imaging techniques can help elucidate how novel agents interact with the tumor target [4], by providing the means to observe how tumors respond, and how efficacious the novel drug is on a case-by-case basis. If translated to patients, this could provide additional information beyond simple diagnosis of disease, such as an indication of the interaction between tumor and host microenvironment, which coupled with monitoring of therapeutic response, could provide a personalised medicine approach to therapy [5]. One class of cancer therapeutics that would benefit greatly from visualisation of the tumor microenvironment is that of Vascular Targeted Agents (VTAs). VTAs target tumor blood vessels with the intent of either destroying existing tumor vasculature (Vascular Disrupting Agents; VDAs) or inhibiting any further growth of the tumor vascular network (Angiogenesis Inhibitors; AIs) [6]. Several VDAs, including OXi4503 (Combretastatin A1-diphosphate) employed in the current study, have been used in clinical trials for treating a wide range of solid tumors, including NSCLC, prostate, ovarian, and anaplastic thyroid [7, 8]. It would therefore be advantageous to observe the effect of VTA action on tumor blood vasculature *in situ*. *Ex vivo* analysis of tumor vasculature using histochemical methods is a powerful technique, but requires large cohorts of animals for significant results and cannot be used to study the same tumors in a longitudinal manner [9]. Intravital microscopy is commonly used to provide high resolution images of tumor growth and vasculature, but typically requires either contrast agents or labelled cells, can only visualise small tumors or partial volumes, and is either an invasive terminal procedure or requires the implantation of a surgical window to replace the highly scattering skin layer [10]. Tumor vascularisation can be assessed by ultrasound without surgical exposition, however visualisation of microvascular change is limited without the use of micro-bubble contrast agents [11]. Likewise, Magnetic Resonance Imaging [12] and Computed Tomography (CT) angiography [13] can provide images of the vasculature of whole tumors but both require the use of contrast agents to obtain high-resolution images. In addition, high-resolution micro-CT [14] requires high X-ray doses limiting the number of repeat measurements in longitudinal studies. Another technique capable of evaluating tumor vascular function after VTA treatment is dynamic Bioluminescent Imaging (BLI) [15]; BLI is straightforward to implement and capable of high-throughput, but lacks the spatial resolution to visualise tumor vasculature, and requires transfection of cell lines used and administration of exogenous substrate.

Photoacoustic imaging (PAI) is an emerging non-invasive technique that offers the prospect of overcoming these limitations [16–19]. It relies on the generation of ultrasound waves through the absorption of low-energy non-ionizing laser pulses by light absorbing molecules, such as haemoglobin. By detecting the time-of-arrival of these waves at the tissue surface, an image of the internal tissue structure can be reconstructed. Since PA image contrast is based on optical absorption, and haemoglobin absorbs light strongly at visible and near infrared wavelengths, the microvasculature can be visualised with excellent visibility without employing exogenous contrast. Moreover, since the contrast is encoded on to acoustic waves, which are scattered much less than photons, PAI avoids the depth and spatial resolution limitations of purely optical imaging techniques such as intravital microscopy: with PAI, cm scale penetration depths with scalable spatial resolution ranging from tens to hundreds of micrometres (depending on depth) are achievable. Additionally, there is the potential to acquire functional information via the measurement of both blood oxygen saturation [18] and flow [20]. These factors offer the prospect of high resolution label-free 3D imaging of whole subcutaneous tumor vascular morphology and function in an entirely non-invasive manner [21–25], thus making PAI a promising tool for longitudinal studies of VTA action. The assessment of response to VTA based treatment in preclinical models has been demonstrated in several preliminary PAI studies; Bohndiek et al have shown antiangiogenic therapy can be observed to normalise tumor vasculature and regress growth of early vessel formation [24], whilst early feasibility studies have shown that PAI can visualise the short term response to VDA based treatment at one time point and for a single dose [23, 25, 26], and multiple time points within 6 hours [27] and 24 hours post VDA treatment [28].

In the current study, we advance previously reported research on VDA-based therapy assessed by PAI by investigating the effects of the VDA OXi4503 at multiple time points over 16 days on two colorectal xenografts with differing vascular architecture and pathophysiology [29, 30]. We also compare the vascular effects of a range of OXi4503 doses in the same tumor models. A key requirement was the ability to visualise the often subtle changes in tumor vascular morphology produced by the VDA, particularly in poorly vascularised tumors or with low dose therapy. This was made possible by using a custom-designed high resolution PA scanner based on all-optical detection which provides more detailed 3D images than conventional piezoelectric based PA scanners previously used for tumor imaging studies. Using this system, we show how PAI provides a detailed assessment of the evolution of the VDA-induced vascular destruction-regrowth cycle, the relationship between baseline tumor vascular pathophysiology and treatment response, and the effect of dose on pharmacodynamic response.

Materials and method

Photoacoustic imaging system description

An all-optical photoacoustic scanner based on a Fabry-Perot (FP) polymer film ultrasound sensor was used to image the mice in widefield tomography mode [19]. A schematic of the system is shown in figure 1. Its operating principles have been described in detail previously [23, 31, 32]. Briefly, it consists of a tunable optical parametric oscillator (OPO) laser system

(Quanta Ray Pro-270/premiScan, Newport Spectra Physics/GWU Lasertechnik – not shown) which generates 7 ns excitation laser pulses at a pulse repetition frequency (PRF) of 50Hz. The output of the laser is coupled into an optical fibre which produces a divergent beam that forms a large diameter (~2cm) spot on the FP sensor. The beam is then transmitted through the sensor head and into the adjacent tissue where it is absorbed producing broadband acoustic waves at ultrasonic frequencies. These waves propagate back to the sensor where they are detected at different spatial points and used to reconstruct a 3D image.

The sensor itself is a multilayer thin film structure comprising two dichroic mirrors separated by a 22 μm thick polymer spacer thus forming a FP etalon. The mirrors are designed to be highly reflective between 1500nm and 1600 nm but transparent to wavelengths between 590nm to 1200 nm to permit transmission of the excitation laser wavelength (640nm in this study) through the sensor head. The photoacoustic waves generated in the tissue arrive at the FP sensor where they modulate its optical thickness. This produces a corresponding time-varying change in reflectivity which is read-out using a 1550 nm interrogation laser beam that is focussed on to the surface of the FP sensor. Forming a 3D image requires recording the spatial distribution of the incident photoacoustic waves over the surface of the sensor. This is achieved by optically scanning the interrogation beam point-by-point over an area on the sensor using a galvanometer based x-y scanner. At each scan point, a time-resolved photoacoustic waveform is acquired in response to a single laser pulse. In this study, the scan area was 14mm x 14mm, the step size was 100μm and the element size (defined to a first approximation as the FWHM diameter of the focussed interrogation beam) was 60μm. For each scan, ~20,000 waveforms, each containing 800 time samples with a temporal sampling interval of 10 ns, were acquired without signal averaging and using an incident laser fluence of 5mJ/cm^2, which is below the maximum permitted exposure for human skin [33]. All images were acquired using an excitation wavelength of 640nm as this was found to provide an acceptable compromise between contrast and penetration depth. The sensor provides a broadband frequency response with a -3dB bandwidth of 39 MHz [31].

Image reconstruction, visualisation and quantitation

3D photoacoustic images were reconstructed from the acquired waveforms, using a time reversal algorithm [34] with a correction for acoustic attenuation in tissue implemented using a time variant filtering method [35]. The image reconstruction algorithm was implemented using k-Wave, an open source MATLAB toolbox developed at University College London for the time-domain simulation and reconstruction of PA and ultrasound wave fields (www.k-wave.org) [36]. Before reconstruction, the detected raw photoacoustic signals, arranged in a grid of size 141 x 141 x 800, were interpolated onto a three times finer x–y grid of size 423 x 423 x 800. The sound speed used in the reconstruction was selected using an autofocus approach, based on a metric of image sharpness [37]. An exponential function normalisation with respect to depth was applied to the reconstructed image data set as a first-order correction for the effect of optical attenuation to aid visualisation. All images are displayed as maximum intensity projections (MIPs) of the reconstructed 3D image data sets. In a lateral x-y MIP of a PA image data set, subsurface anatomy can be obscured by the large PA signal generated in the skin due to its strong optical absorption. Unless otherwise

stated therefore, the skin contribution was removed by computing all x-y MIPs over the depth range z = 1 - 6 mm, thereby excluding contrast for depths below 1mm.

In order to quantify changes in the tumor signal produced by the VDA, the tumor was manually segmented from the reconstructed PA image. The segmentation was implemented by viewing the 3D image data set and applying a mask created by tracing a boundary around the widest cross section of the tumor in the lateral view. The mean signal intensity of all voxels above the noise floor in the segmented image was then obtained, with the noise floor chosen to be the 10th percentile of signal intensities of voxels within the segmented region.

System imaging performance

The system provides a 14mm x 14mm lateral field-of-view, a penetration depth of approximately 10mm and lateral and vertical resolutions in the range 50-150μm, depending on x-y position and depth. The total acquisition time is approximately 7 minutes, limited by the 50Hz PRF of the excitation laser. An illustration of the *in vivo* imaging performance of the system is provided in figure 1b. This shows an example image of a subcutaneous SW1222 tumor xenograft implanted in the mouse flank acquired using an excitation wavelength of 640nm. The images are displayed as lateral (x-y) and vertical (x-z and y-z) MIPs of the reconstructed 3D image data set; the x-y MIP was computed for the depth range z =0 – 8mm, thus the top 1mm was not removed in this specific example. An animated volume rendered image is also available online (Video 1) which further illustrates the 3D nature of the image data set. The tumor is clearly visualised in the centre of the x-y MIP (as indicated by yellow arrows) with normal vasculature surrounding it. The central region of the tumor exhibits relatively uniform albeit somewhat granulated contrast. This is broadly consistent with previous studies [23] which have shown that this tumor type exhibits a dense, homogeneously distributed vasculature with sub-resolution vessel spacing; hence, in this example, the tumor core is represented by a region of spatially averaged contrast, rather than a network of individually resolvable tumor vessels. The vertical x-z and y-z MIPs also show the tumor core and the surrounding non-tumor vessels and demonstrate that it is possible to visualise the full thickness of the tumor. The system can thus image an entire subcutaneous tumor and its host environment non-invasively with high resolution in 3D to a depth of up to 8mm as required for this study.

Animal models

All *in vivo* experiments were performed in accordance with UK ‘Animals Scientific Procedures act’ (1986) and adhered to the Workman P *et al* [38] ‘Guidelines for the welfare and use of animals in cancer research’. Female nu/nu CD1 mice between the ages of 8-10 weeks were acquired from Charles River Laboratories and housed in barrier conditions within individual ventilated cages with food and water *ad libitum.* Two human colorectal carcinoma cell lines SW1222 and LS174T [29, 30] were used to establish xenografts on account of their different vascular architectures (the former being well vascularised while the latter has a poorer and more heterogeneous blood supply) enabling the influence of tumor blood supply on therapeutic response to be studied. Cell lines were tested negative for mycoplasma using in-house Polymerase Chain Reaction. The cells were prepared through sterile tissue culture techniques to a concentration of $5x10^6$ per 100μl of serum free media.

A 100μl bolus of cells was injected subcutaneously into the right flank of the animals, with subsequent tumor growth measured using digital callipers and tumor volume calculated using the ellipsoid formula [39]:

$$v = LxBxHx\left(\frac{\pi}{6}\right)$$

Experimental design

Tumors were size-matched to maintain similar volumes across groups, with an overall range of diameters between 6mm and 8mm. For dosing, a stock concentration of OXi4503 was prepared in sterile saline and animals injected i.v. at a ratio of 10ml/kg. Total drug administered was dependent on the stock concentration used, with the volume of i.v. dose kept at 10ml/kg. The mice were scanned by placing them on the FP sensor head and inserting a drop of water between the skin and the sensor to provide acoustic coupling.

Two studies were undertaken; the first investigated the long term action of the VDA on the vasculature of both tumor types over an extended period of 16 days, a time period sufficient to observe the expected tumor blood vessel destruction and regrowth cycle. From here on, this is termed the ‘vessel regrowth’ study. The second study evaluated the response of the two different tumor pathologies to differing levels of drug dosage. From here on this is referred to as the ‘Dose response’ study. For the vessel regrowth studies, n=4 SW1222 and LS174T tumors were imaged at baseline before intravenously administering a single 40mg/kg dose of OXi4503. Subsequent imaging was performed at day 1, 2, 3, 6, 9, 13 and 16 post-dose along with calliper measurements of tumor volume. For the dose response arm of the experiment, groups consisted of n≥4 animals for both cell lines at concentrations of OXi4503 of 40mg/kg, 10mg/kg and 1mg/kg, with a saline sham control. These groups were imaged at baseline and day 2 post dose, as this was the expected point of greatest response to treatment based on previous studies using OXi4503 [40].

Statistical analysis

Statistical analysis of the data was performed using Matlab. All values are reported as mean ± standard error. For the tumour regrowth study, the change in PA signal, over the duration of the study, in the SW1222 and LS174T mice (n = 4 each) was tested for statistical significance difference using a two tailed Mann-Whitney test. In addition, a Pearson correlation analysis was used to determine the correlation between change in PA signal and change in tumour volume measured with callipers. For the dose response study, we carried out a one-way ANOVA Ominibus test on the means of the four treatment groups, 40mg/kg, 10mg/kg, 1mg/kg and control. Further *post hoc* pairwise multiple comparison tests were used to examine differences between individual paired groups, using Fisher’s modified least significant difference test (Fisher-Hayter). For all statistical tests the significance level was $p < 0.1$.

Results

For the re-growth study, mice with SW1222 and LS174T tumors were dosed with 40mg/kg OXi4503 and imaged longitudinally over 16 days to study the effect of the drug on the tumor

signal. figure 2 shows images (x-y and x-z MIPs) of a subcutaneous SW1222 tumor in the same mouse at different time points over this period. The images show a large central area of signal void by 24 hours post treatment, with a surviving rim of signal observed around the location of the tumor periphery. Over the 16-day time frame observed, this area of signal void gradually reduces as new vasculature re-populates the destroyed central core of the tumor, until it has almost disappeared by day 16. By this time the contrast in this central area has returned to a level that is comparable to the pre-dose image. Broadly similar behaviour, albeit with some variation in the extent and time course of the tumor signal, is observed in a second mouse with an SW1222 tumor (figure 3), and in other SW1222 tumors imaged but not shown. Images acquired over the same time period of two different mice with LS174T tumors are shown in figures 4 and 5. The pre-treatment images in both cases illustrate the more heterogeneous and sparsely distributed vasculature of the LS174T tumor compared to the SW1222 tumor with individual tumor vessels now visible. Post dosing, the reduction in signal is smaller, and its spatial distribution less distinct, than that seen for the SW1222 tumors. In addition, the treated LS174T xenograft tumors shows vessels in a more irregular pattern within the tumor region, with some areas lacking signal and with a less distinct peripheral rim signal to the SW1222 tumors. The near complete absence of signal in the central part of the SW1222 tumor is not so clearly observed in the LS174T tumors, with some small areas of contrast remaining throughout the entire 16 days of the study. Moreover, the extent to which signal returns to the tumor core and re-establishes its baseline spatial distribution over this period is significantly less pronounced than for the SW1222 tumor.

To assess the time-course of the vascular destruction and re-growth quantitatively, the images acquired for each mouse in the study were segmented to isolate the tumor region (see methods). The mean voxel intensity of the segmented region was then estimated and plotted for each time point. This data is shown for both tumor types in figures 6 (a) and (b) alongside corresponding calliper based measurements of tumor volume (figure 6 (c) and (d)). All four SW1222 mice showed a marked decrease in signal of up to 80% over the first 2 days, consistent with the extensive regions of signal void in the tumors in figures 2 and 3. This initial reduction is followed by either an increase ($m1_{SW}$ and $m4_{SW}$) or a prolonged decrease ($m2_{SW}$ and $m3_{SW}$) in PA signal (fig 6), before a period of quiescence is established at around day 6. At approximately 13 days the signal starts to increase due to vessel re-growth, again as clearly observed in figures 2 and 3. The corresponding SW1222 tumor volume measurements in figure 6(c) show an initial reduction in tumor size for all 4 mice, tracking the drop in PA signal. Subsequently, with the exception of $m3_{SW}$ there is no significant growth in tumor volume over the remaining duration of the study.

The PA signal data for the LS174T tumor (figure 6b) show broadly similar behaviour to that of SW1222, although several differences are evident. First, the extent to which the signal drops in the initial vascular destruction phase over the first 2 days is less pronounced than for the SW1222 tumors. The exception is $m3_{LS}$ which shows a large spike (possibly due to a blood pool/clot), that appeared 24 hours after treatment and then plateaus out. Second, the extent to which the signal increases in the vessel re-growth phase (>12 days) is less evident between mice; $m1_{LS}$ and $m3_{LS}$ appear to show a modest increase in PA signal that could be indicative of vessel regrowth whereas $m2_{LS}$ and $m4_{LS}$ exhibit a prolonged quiescent phase which extends to the study endpoint at day 16. Differences between the two tumor types are

most evident in the tumor volume measurements (figure 6 c&d) and their accompanying PA signal. While three of the four LS174T tumors showed a small reduction in size over the initial 4 days (figure 6d), they did not exhibit the prolonged arrested growth of the SW1222 tumors (figure 6(c)) which appears to track the PA signal in most cases. The LS174T tumor volume of each mouse increases significantly beyond day 6 until the study endpoint, whilst the PA vascular signal (figure 6(b)) remains either constant or exhibits only a small increase.

For a statistical comparison of the extent of signal reduction and return in the SW1222 and LS174T during the study, the average signal reduction over 16 days was calculated for each mouse. The mean signal reduction in the SW1222 mice (n=4) was 52.7 ± 8.80, while the corresponding reduction in the LS174T mice (n = 4) was 32.1 ± 10.3. A two tailed Mann-Whitney test shows a statistically significant difference in the reductions in PA signal between the two groups ($p = 0.057$), consistent with the qualitative and quantitative differences in figure 6 a-b. To test for a correlation between the PA signal (figure 6a & b) and the tumour volume (figure 6c & d), at each time point both parameters were averaged for the four mice in each group. Using a Pearson correlation analysis, there was a strong positive correlation found between the PA signal reduction and the tumor volume measured by callipers for the SW tumors (r = 0.744, p = 0.055). For the LS tumors, there was no correlation (r = -0.02, p = 0.9636).

The second arm of the study, the dose response to OXi4503, was undertaken by comparing images acquired for doses of 40mg/kg with 10mg/kg, 1mg/kg, and a saline sham control, with the results shown in figure 7. This figure shows x-y MIP images of all dose levels after dosing with OXi4503. The left hand panel shows representative SW1222 tumors whilst the right hand panel shows LS174T tumors. Both panels show baseline and 48 hours post dose within the same tumor, with the tumor location indicated by the yellow arrows in the pre-dose images. In SW1222 tumors, doses of 40mg/kg and 10mg/kg produced the characteristic central tumor signal void, whilst the dose of 1mg/kg produced a small but still visually discernible reduction in signal compared with sham treated controls. In LS174T tumors only the 40mg/kg and 10mg/kg doses produce a notable effect, with the 1mg/kg dose being comparable to saline control in which no visually discernible effect was observed. To assess the dose response quantitatively, the tumor regions on the images for each mouse were segmented as described previously. The percentage reduction in mean voxel intensity from the corresponding pre-dose baseline image was estimated and plotted for each dose and the control as shown in figure 7(b). For the SW1222 tumors, mean reductions of 60%, 52% and 20% of medial PA signal intensity from baseline are observed for 40mg/Kg, 10mg/Kg and 1mg/Kg groups respectively. For the LS174T tumor smaller reductions of 30%, 26% and 4% are evident.

Using an ANOVA omnibus test, we found that for both the SW1222 and LS174T tumours, there was a statistically significant difference between the mean changes in PA signal from baseline to 48hrs of the dose groups. ANOVA ($F(3,14) = 10.17$, $p = 0.0008$) for SW1222 and ANOVA ($F(3,11) = 4.35$, $p = 0.03$) for LS174T. We then conducted *post hoc* pairwise multiple comparison tests to examine differences between individual paired groups, using Fisher's modified least significant difference test (MLSD: Fisher-Hayter). For the SW1222 tumors, the changes in PA signal within the control group were significantly different from

those within the 10mg/kg group ($p = 0.016$) and 40mg/kg group ($p = 0.001$). Similarly, PA signal changes in the 1mg/kg group were also significantly different from the 10mg/kg group ($p = 0.029$) and 40mg/kg group ($p = 0.0016$). There were no significant differences between the control and 1mg/kg groups, and also between the 10mg and 40mg/kg groups. For the LS174T tumors, statistically significant differences exist between the control group and the 10mg/kg group ($p = 0.043$), and between the control group and the 40mg/kg group ($p = 0.046$). There is no statistically significant difference between other dose group pairs.

Discussion

In this study we have shown that by undertaking serial longitudinal PA imaging studies we can observe the pharmacodynamic response of the tumor vasculature to therapy in a completely non-invasive manner over an extended period of time.

Both the qualitative and quantitative results shown are consistent with previous *ex vivo* histological studies. First, consider the data in figures 2–6 which correspond to the vessel re-growth arm of the study. The initial vascular disruption produced by treatment is denoted by a lack of PA signal in the tumor core. This is clearly seen at the early stages (24 and 48 hours post dose) of response to OXi4503, and is significantly more pronounced in SW1222 tumors compared to LS174T. It can also be seen that the peripheral rim of the SW1222 tumors, most noticeably for mouse $m4_{SW}$ (figure 2), shows a high signal intensity following treatment; this remaining viable rim following treatment by combretastatin compounds is well known through published histological studies [41–43]. The appearance of this rim is a sign of effective tumor-specific vasculature targeting and normal tissue sparing and is probably a consequence of several factors. The first factor is that vessels in the periphery of the tumor have survived through interaction with the surrounding normal tissue that is unaffected by the action of OXi4503, and these vessels have a high coverage of pericytes, promoting stabilisation and making them less responsive to VDAs than the central, less mature vessels [44]. The second is that any inflowing blood no longer has anywhere to go within the necrotic core of the tumor, and pools at the tumor edge, increasing the level of haemoglobin at the rim and therefore the PA signal. This has recently been demonstrated by optical projection tomography in both LS174T and SW1222 xenografts following OXi4503, which also revealed an increase in the size of peripheral vessels after treatment which could be an additional contributing factor to the increased PA rim signal [45]. A third possible reason is the efflux of vascular and cellular debris including absorbing haemoglobin fragments from the destroyed tumor core being pushed to the periphery of the tumor due to interstitial pressure [46]. This necrotic debris has previously been observed by transmission electron microscopy at 24h post treatment with OXi4503 [47].

The initial decrease in PA signal following administration of the VDA can be observed to diminish over time and is indicative of tumor revascularisation. It is visually most noticeable in the SW1222 tumors, especially in figure 2 where the large central void created by the VDA appears to become almost completely repopulated by new vessels from the outside edge of the tumor mass over the 16 days of the study. The PA images also suggest some revascularisation of the LS174T tumors occurs, though compared to the SW1222 tumors this is attenuated, less well defined and exhibits greater variability between mice, a consequence

of the more heterogeneous vasculature exhibited by this tumor. Although the PAI data suggests a degree of revascularisation in all tumors, figures 6 (a) and (b) shows that no tumor of either SW1222 or LS174T returns fully to pre-treatment levels of PA signal.

The difference in response of the SW1222 and LS174T tumours to the VDA is confirmed by a two tailed Mann-Whitney test which shows a statistically significant difference in the average reduction in PA signal over the 16 day duration of the study between the two tumors ($p = 0.057$). The mean signal reduction in the SW1222 mice (n=4) was 52.7 ± 8.80, while the corresponding reduction in the LS174T mice (n = 4) was 32.1 ± 10.3. It is well known that the two tumors have very different vascular states and pathophysiologies [29, 30, 45], with the well oxygenated SW1222 tumors having a more homogeneous distribution of extensive, smaller vessels, while LS174T has a heterogeneous distribution with larger vessels towards the periphery and areas of poor vascularisation, leading to extensive hypoxia. This makes the LS174T more inherently resistant to treatment with VDAs; not only are the larger vessels in the LS174T more mature and therefore more resistant to the drug, but LS174T cells are already more accustomed to hypoxic conditions [30] and thus better adapted to withstand the oxygen deficiency resulting from the VDA-induced vascular destruction. These differences in treatment response are reflected in the PA images. The more extensive and organised the original vascular network the greater the destruction observed, as seen in the PA images of the SW1222 tumors (eg figures 2 and 3); extensive areas of PA signal void correspond to avascular regions within these tumor types following treatment with OXi4503. By contrast, in the more chaotic and heterogeneous vascular architecture found in LS174T tumors (figures 4 and 5) there is a clear decrease in PA signal (figure 6(b)) but it is noticeably attenuated compared to the SW1222 tumors. The initial vascular state of the tumor also impacts on tumor growth. Figures 6(a) and (c) show that, in most cases, the drug-induced reduction in the SW1222 tumor PA signal is matched by an arrest in growth with tumor volumes typically remaining below baseline. A strong positive correlation was found between the reduction in PA signal and the measured tumour volume at each time point ($r = 0.744$, $p = 0.055$). By contrast, figure 6(d) suggests that LS174T tumor growth continues following an initial week of inhibition, despite the relative quiescence of the corresponding PA signal which suggests that the drug is continuing to inhibit vascular growth (figure 6(b)). Indeed, there was no correlation found between the PA signal reduction and tumour volume ($r = -0.02$, $p = 0.9636$).

Having shown that PAI can visualise major vascular disruption following treatment with a high dose of OXi4503, it is also notable that PAI can detect smaller changes in vascular disruption within the tumor, as demonstrated by reduced doses of the VDA. figure 7 shows the effect of OXi4503 treatment at 40mg/kg, 10mg/kg, 1mg/kg, and saline sham control at baseline and 48hrs for PA imaging in SW1222 and LS174T tumors. Again, the effect on LS174T tumors appears much less pronounced than in SW1222 tumors. In the case of the LS174T tumors, *post hoc* pairwise multiple comparison tests shows a statistically significant difference between the vascular changes in the control group and the 10mg/kg group ($p = 0.043$), and between the control group and the 40mg/kg group ($p = 0.046$). There is no statistically significant difference between other group pairs. However, for the SW1222 tumors, there is a statistically significant difference between the control group and the 10mg/kg group ($p = 0.016$), control group and 40mg/kg group ($p = 0.001$), 1mg/kg group

and 10mg/kg group ($p = 0.029$), and between the 1mg/kg group and the 40mg/kg group ($p = 0.0016$). These results are consistent with Hill et al [35] who also found a dose-dependent response to OXi4503. We show here that measures of PAI can distinguish between effective (10mg/kg and 40mg/kg) and non-effective (1mg/kg) doses of the same vascular disrupting drug, based on image assessment compared to baseline data.

In the current study, it has been assumed that the PA signal at 640nm provides a measure of total haemoglobin. In practice, at this wavelength, the signal is also sensitive to changes in blood oxygen saturation (SO_2). This is a potentially confounding factor; for example, if the tumour SO_2 decreases over time, the PA signal at 640nm will increase leading to an underestimation of the VDA-induced vascular destruction. However the spatial-temporal distribution of the signal in both arms of the study is consistent with the known VDA response of the tumour models used [40, 48]suggesting that interpreting the PA signal as a marker primarily of tumour vascularisation is reasonable in the context of the current study. Nevertheless, the potential for error due to SO_2 changes is recognised, particularly in terms of image quantification, the extent of which could be assessed in future by acquiring images at the SO_2 independent 808nm isobestic wavelength for comparison.

This study has demonstrated that the FP based PA scanner can provide high resolution images of deep (≈8mm) subcutaneous tumors at a higher quality than conventional piezoelectric based scanners. This is a consequence of the optical transduction mechanism it employs which provides a broadband frequency response, fine spatial sampling and acoustically small element size all of which are important for an accurate image reconstruction. Additional factors contributing to the high image quality include the methods employed to mitigate the effects of acoustic attenuation, identifying the optimal sound speed and the use of an optimised reconstruction algorithm based on time-reversal. A current limitation however is the relatively slow acquisition speed (~7 minutes), a consequence of the sequential manner in which the sensor is addressed and the relatively low PRF of the excitation laser. There is the potential to reduce this significantly and acquire 3D images in a few seconds by increasing the laser PRF, parallelising the detection scheme [49], and employing compressed sensing techniques [50]. Other anticipated technical advances include the development of methods for acquiring functional images of blood oxygen saturation using spectroscopic methods [18] and blood flow via the PA Doppler effect [20]. Although both methods still require further development for use at multi-mm or cm scale depths relevant to imaging whole tumors, they offer the additional prospect of studying tumor hypoxia and the role it plays in VTA based therapeutic response.

Whilst this study has focussed on the use of PAI as a preclinical imaging tool, the technology and the results obtained in the current study are translatable to the clinic with a number of PA scanners currently being developed or evaluated for the clinical assessment of a variety of cancers including breast, prostate and ovarian cancer [51]. The visualisation of vascular destruction and revascularisation following treatment observed in the current study could be beneficial in clinical practice. For example, monitoring the time to regrowth could prove significant in the personalised clinical scheduling of repeat-dose treatment. In cases where the vessel regrowth originates from the surviving rim, specific targeting of the rim with combination therapies and using PAI to monitor the effect on the tumor could be

Europe PMC Funders Author Manuscripts

advantageous in optimising treatment parameters. The ability to observe differences in vascular pathophysiology, which affects outcome to treatment with VDAs, could potentially be used to assess initial tumor vascular state, and therefore expected outcome, in different patients. The observation of the pharmacodynamic effect of VDA action will allow personalised dose scheduling for subsequent treatments. Moreover, the use of functional PAI for the assessment of tumor hypoxia could yield a further predictor of response to specific therapies to help tailor, plan and monitor treatment.

This study demonstrates the applicability of PAI for the evaluation of cancer therapy based on the use of vascular disrupting agents (VDAs). Using a custom-designed scanner, we have shown that high resolution 3D images of the vascular morphology of whole subcutaneous tumors can be acquired longitudinally, non-invasively, and without use of exogenous contrast agents. The high quality of the acquired images and their three dimensional nature has been key to this endeavour, enabling the detection of subtle spatial-temporal vascular changes in response to the VDA. This capability has been exploited to determine the comparative initial effects of OXi4503 action on the different vascular architecture of two colorectal tumor models, and the subsequent patterns of vascular regrowth. The influence of their different vascular pathophysiologies on treatment response over 16 days, and the effect of different doses of OXi4503, is described. In doing so we have demonstrated, for the first time in a longitudinal, non-invasive manner, that the tumor regrows inwards from the surviving rim. PAI was also used to show that highly vascularised SW1222 tumors exhibit both greater initial vascular destruction in response to OXi4503 and a more pronounced subsequent long term revascularisation than the LS174T tumors, which possess a more sparsely distributed heterogeneous vasculature. In addition, we have shown that PA imaging is able to differentiate between the effects of different doses of OXi4503. Whilst this study has concentrated on tumor response to VDA treatment, other vascular targeted agents such as anti-angiogenic therapies using humanised antibodies [52], and small molecules that attempt to normalise the tumor vascular microenvironment [53], would also be prime candidates for investigation with PAI.

In summary, we have demonstrated that PA imaging is a powerful preclinical tool for studying the tumor response to vascular disrupting therapy. Moreover, PA imaging is well suited to clinical use, and the translational aspect of the current study offers new opportunities for personalised clinical medicine in terms of predicting the response to therapy, and determining the most suitable dosing strategies for individual patients.

Supplementary Material

Refer to Web version on PubMed Central for supplementary material.

Acknowledgements

The VDA OXi4503 (combretastatin A1-diphosphate/CA1P), currently in clinical trial for cancer treatment (NCT02576301), was a kind gift from Dr David Chaplin (Mateon Therapeutics, San Francisco, USA). This work was also supported by King's College London and University College London Comprehensive Cancer Imaging Centre, Cancer Research UK and the Engineering and Physical Sciences Research Council (EPSRC), in association with the Medical Research Council and Department of Health, UK (C1519/A10331) and ERC Advanced Grant Ref: 741149

References

1. Collins I, Workman P. New approaches to molecular cancer therapeutics. Nature Chemical Biology. 2006; 2:689. [PubMed: 17108987]
2. Mak IW, Evaniew N, Ghert M. Lost in translation: animal models and clinical trials in cancer treatment. Am J Transl Res. 2014; 6(2):114–8. [PubMed: 24489990]
3. de Jong M, Maina T. Of mice and humans: are they the same?--Implications in cancer translational research. J Nucl Med. 2010; 51(4):501–4. [PubMed: 20237033]
4. de Jong M, Essers J, van Weerden WM. Imaging preclinical tumour models: improving translational power. Nat Rev Cancer. 2014; 14(7):481–93. [PubMed: 24943811]
5. Medical imaging in personalised medicine: a white paper of the research committee of the European Society of Radiology (ESR). Insights into Imaging. 2015; 6(2):141–155. [PubMed: 25763994]
6. Siemann DW, Horsman MR. Vascular targeted therapies in oncology. Cell and tissue research. 2009; 335(1):241–248. [PubMed: 18752004]
7. Spear MA, et al. Vascular disrupting agents (VDA) in oncology: advancing towards new therapeutic paradigms in the clinic. Curr Drug Targets. 2011; 12(14):2009–15. [PubMed: 21777190]
8. Patterson DM, et al. Phase I clinical and pharmacokinetic evaluation of the vascular-disrupting agent OXi4503 in patients with advanced solid tumors. Clin Cancer Res. 2012; 18(5):1415–25. [PubMed: 22235096]
9. Nico B, et al. Evaluation of microvascular density in tumors: pro and contra. Histol Histopathol. 2008; 23(5):601–7. [PubMed: 18283645]
10. Lehr HA, et al. Dorsal skinfold chamber technique for intravital microscopy in nude mice. Am J Pathol. 1993; 143(4):1055–62. [PubMed: 7692730]
11. Zhang P, et al. Quantitative Evaluation of Combretastatin A4 Phosphate Early Efficacy in a Tumor Model with Dynamic Contrast-Enhanced Ultrasound. Ultrasound in Medicine & Biology. 2018; 44(4):840–852. [PubMed: 29395676]
12. Fink C, et al. High-resolution three-dimensional MR angiography of rodent tumors: morphologic characterization of intratumoral vasculature. J Magn Reson Imaging. 2003; 18(1):59–65. [PubMed: 12815640]
13. Kiessling F, et al. Volumetric computed tomography (VCT): a new technology for noninvasive, high-resolution monitoring of tumor angiogenesis. Nat Med. 2004; 10(10):1133–8. [PubMed: 15361864]
14. Clark DP, Badea CT. Micro-CT of rodents: state-of-the-art and future perspectives. Physica medica : PM : an international journal devoted to the applications of physics to medicine and biology : official journal of the Italian Association of Biomedical Physics (AIFB). 2014; 30(6):619–634.
15. Liu L, et al. Tubulin-Destabilizing Agent BPR0L075 Induces Vascular-Disruption in Human Breast Cancer Mammary Fat Pad Xenografts. PLOS ONE. 2012; 7(8) e43314 [PubMed: 22937031]
16. Wang LV, Hu S. Photoacoustic Tomography: In Vivo Imaging from Organelles to Organs. Science. 2012; 335(6075):1458. [PubMed: 22442475]
17. Wang LV, Yao J. A practical guide to photoacoustic tomography in the life sciences. Nature Methods. 2016; 13:627. [PubMed: 27467726]
18. Cox B, et al. Quantitative spectroscopic photoacoustic imaging: a review. J Biomed Opt. 2012; 17(6) 061202 [PubMed: 22734732]
19. Beard P. Biomedical photoacoustic imaging. Interface Focus. 2011; 1(4):602–31. [PubMed: 22866233]
20. Brunker J, Beard P. Velocity measurements in whole blood using acoustic resolution photoacoustic Doppler. Biomedical optics express. 2016; 7(7):2789–2806. [PubMed: 27446707]
21. Rich LJ, Seshadri M. Photoacoustic monitoring of tumor and normal tissue response to radiation. Scientific Reports. 2016; 6 21237 [PubMed: 26883660]
22. Ermolayev V, et al. Simultaneous visualization of tumour oxygenation, neovascularization and contrast agent perfusion by real-time three-dimensional optoacoustic tomography. Eur Radiol. 2016; 26(6):1843–51. [PubMed: 26334513]

23. Laufer J, et al. In vivo preclinical photoacoustic imaging of tumor vasculature development and therapy. J Biomed Opt. 2012; 17(5) 056016 [PubMed: 22612139]
24. Bohndiek SE, et al. Photoacoustic Tomography Detects Early Vessel Regression and Normalization During Ovarian Tumor Response to the Antiangiogenic Therapy Trebananib. J Nucl Med. 2015; 56(12):1942–7. [PubMed: 26315834]
25. Bar-Zion A, et al. Functional Flow Patterns and Static Blood Pooling in Tumors Revealed by Combined Contrast-Enhanced Ultrasound and Photoacoustic Imaging. Cancer Res. 2016; 76(15):4320–31. [PubMed: 27325651]
26. Rich LJ, Seshadri M. Photoacoustic Imaging of Vascular Hemodynamics: Validation with Blood Oxygenation Level-Dependent MR Imaging. Radiology. 2015; 275(1):110–118. [PubMed: 25423146]
27. Balasundaram G, et al. Noninvasive Anatomical and Functional Imaging of Orthotopic Glioblastoma Development and Therapy using Multispectral Optoacoustic Tomography. Translational oncology. 2018; 11(5):1251–1258. [PubMed: 30103155]
28. Dey S, et al. The vascular disrupting agent combretastatin A-4 phosphate causes prolonged elevation of proteins involved in heme flux and function in resistant tumor cells. Oncotarget. 2017; 9(3):4090–4101. [PubMed: 29423106]
29. El Emir E, et al. Predicting response to radioimmunotherapy from the tumor microenvironment of colorectal carcinomas. Cancer Res. 2007; 67(24):11896–905. [PubMed: 18089820]
30. Folarin AA, et al. Three-dimensional analysis of tumour vascular corrosion casts using stereoimaging and micro-computed tomography. Microvasc Res. 2010; 80(1):89–98. [PubMed: 20303995]
31. Zhang E, Laufer J, Beard P. Backward-mode multiwavelength photoacoustic scanner using a planar Fabry-Perot polymer film ultrasound sensor for high-resolution three-dimensional imaging of biological tissues. Applied Optics. 2008; 47(4):561–577. [PubMed: 18239717]
32. Jathoul AP, et al. Deep in vivo photoacoustic imaging of mammalian tissues using a tyrosinase-based genetic reporter. Nature Photonics. 2015; 9:239.
33. British standard: safety of laser products BS EN 60825-1. 1994
34. Bradley ET, Edward ZZ, Cox BT. Photoacoustic tomography in absorbing acoustic media using time reversal. Inverse Problems. 2010; 26(11) 115003
35. E Treeby B. Acoustic attenuation compensation in photoacoustic tomography using time-variant filtering. 2013; 18 36008
36. Treeby BE, Cox BT. k-Wave: MATLAB toolbox for the simulation and reconstruction of photoacoustic wave fields. J Biomed Opt. 2010; 15(2) 021314 [PubMed: 20459236]
37. Treeby BE, et al. Automatic sound speed selection in photoacoustic image reconstruction using an autofocus approach. J Biomed Opt. 2011; 16(9) 090501 [PubMed: 21950905]
38. Workman P, et al. Guidelines for the welfare and use of animals in cancer research. Br J Cancer. 2010; 102(11):1555–77. [PubMed: 20502460]
39. Tomayko MM, Reynolds CP. Determination of subcutaneous tumor size in athymic (nude) mice. Cancer Chemother Pharmacol. 1989; 24(3):148–54. [PubMed: 2544306]
40. Salmon HW, Siemann DW. Effect of the second-generation vascular disrupting agent OXi4503 on tumor vascularity. Clin Cancer Res. 2006; 12(13):4090–4. [PubMed: 16818709]
41. El-Emir E, et al. Tumour parameters affected by combretastatin A-4 phosphate therapy in a human colorectal xenograft model in nude mice. Eur J Cancer. 2005; 41(5):799–806. [PubMed: 15763657]
42. Chaplin DJ, Pettit GR, Hill SA. Anti-vascular approaches to solid tumour therapy: evaluation of combretastatin A4 phosphate. Anticancer research. 1999; 19(1A):189–195. [PubMed: 10226542]
43. Pedley RB, et al. Eradication of colorectal xenografts by combined radioimmunotherapy and combretastatin a-4 3-O-phosphate. Cancer Res. 2001; 61(12):4716–22. [PubMed: 11406542]
44. Chen M, et al. Pericyte-targeting prodrug overcomes tumor resistance to vascular disrupting agents. The Journal of Clinical Investigation. 2017; 127(10):3689–3701. [PubMed: 28846068]

45. d'Esposito A, et al. Computational fluid dynamics with imaging of cleared tissue and of in vivo perfusion predicts drug uptake and treatment responses in tumours. Nature Biomedical Engineering. 2018; 2(10):773–787.

46. Tozer GM, Kanthou C, Baguley BC. Disrupting tumour blood vessels. Nat Rev Cancer. 2005; 5(6):423–35. [PubMed: 15928673]

47. Pedley, RB, Tozer, GM. The Use of Animal Models in the Assessment of Tumour Vascular Disrupting Agents (VDAs)Vascular Disruptive Agents for the Treatment of Cancer. Meyer, T, editor. Springer New York; New York, NY: 2010. 49–75.

48. Chan LS, et al. Effect of vascular targeting agent Oxi4503 on tumor cell kinetics in a mouse model of colorectal liver metastasis. Anticancer Res. 2007; 27(4b):2317–23. [PubMed: 17695520]

49. Huynh, N, , et al. Sub-sampled Fabry-Perot photoacoustic scanner for fast 3D imagingSPIE BiOS. SPIE: 2017.

50. Simon A, et al. Accelerated high-resolution photoacoustic tomography via compressed sensing. Physics in Medicine & Biology. 2016; 61(24):8908. [PubMed: 27910824]

51. Valluru KS, Wilson KE, Willmann JK. Photoacoustic Imaging in Oncology: Translational Preclinical and Early Clinical Experience. Radiology. 2016; 280(2):332–49. [PubMed: 27429141]

52. Shahneh FZ, et al. Tumor angiogenesis and anti-angiogenic therapies. Hum Antibodies. 2013; 22(1-2):15–9. [PubMed: 24284305]

53. Goel S, et al. Normalization of the vasculature for treatment of cancer and other diseases. Physiol Rev. 2011; 91(3):1071–121. [PubMed: 21742796]

Europe PMC Funders Author Manuscripts

Europe PMC Funders Author Manuscripts

Statement of translational relevance

Advanced assessment of response to therapy is required if the goal of personalised medicine is to be achieved. With regards to vascular targeted therapies, photoacoustic imaging (PAI) is a powerful tool to assess response of tumour vasculature to drug intervention. PAI is completely non-invasive and non-ionising, therefore the translation to the clinic is eminently achievable. The current manuscript is highly relevant to this translational effort as it demonstrates the clinical rationale for implementing PAI in the clinic, namely the ability to monitor the pharmacodynamic response to treatment. This is presented longitudinally and at different doses of drug in two different in vivo models of tumour vascularisation. This is pertinent to the clinical setting as it replicates different vascular states within patients, shows the ability of PAI to monitor the full cycle of drug action and relapse leading to return of tumour growth, and the utility of PAI in the establishment of effective levels of drug treatment.

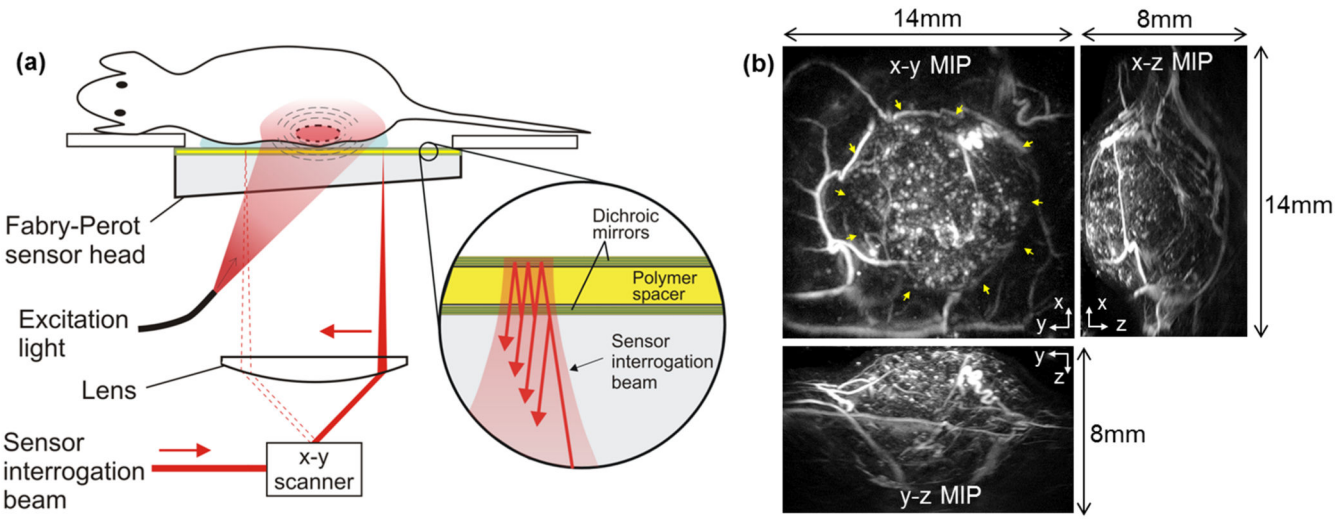

Figure 1. Fabry-Perot-based photoacoustic scanner and example image of a subcutaneous tumor xenograft.

(a) scanner architecture. Excitation laser pulses are transmitted through the FP sensor head and absorbed in the tissue generating photoacoustic signals which are then detected by the Fabry-Perot polymer film ultrasound sensor. Inset: an expanded view of the sensor which comprises a polymer spacer sandwiched between a pair of dichroic mirrors that are transparent to the excitation laser wavelength but highly reflective to the sensor interrogation beam wavelength. The sensor operates by raster scanning a focused continuous wave interrogation laser beam across it and measuring the change in the power of the reflected beam produced by acoustically-induced changes in the polymer spacer thickness. (b) Photoacoustic image of SW1222 tumor xenograft acquired using the scanner and displayed (clockwise) as x-y, x-z and y-z maximum intensity projections (MIPs). An animated volume rendered representation of this data can be viewed online (Video 1. The yellow arrows on the x-y MIP indicate the tumor. The x-z and y-z MIPs show that the entire tumor can be visualised with high resolution to a depth of approximately 8mm.

Europe PMC Funders Author Manuscripts

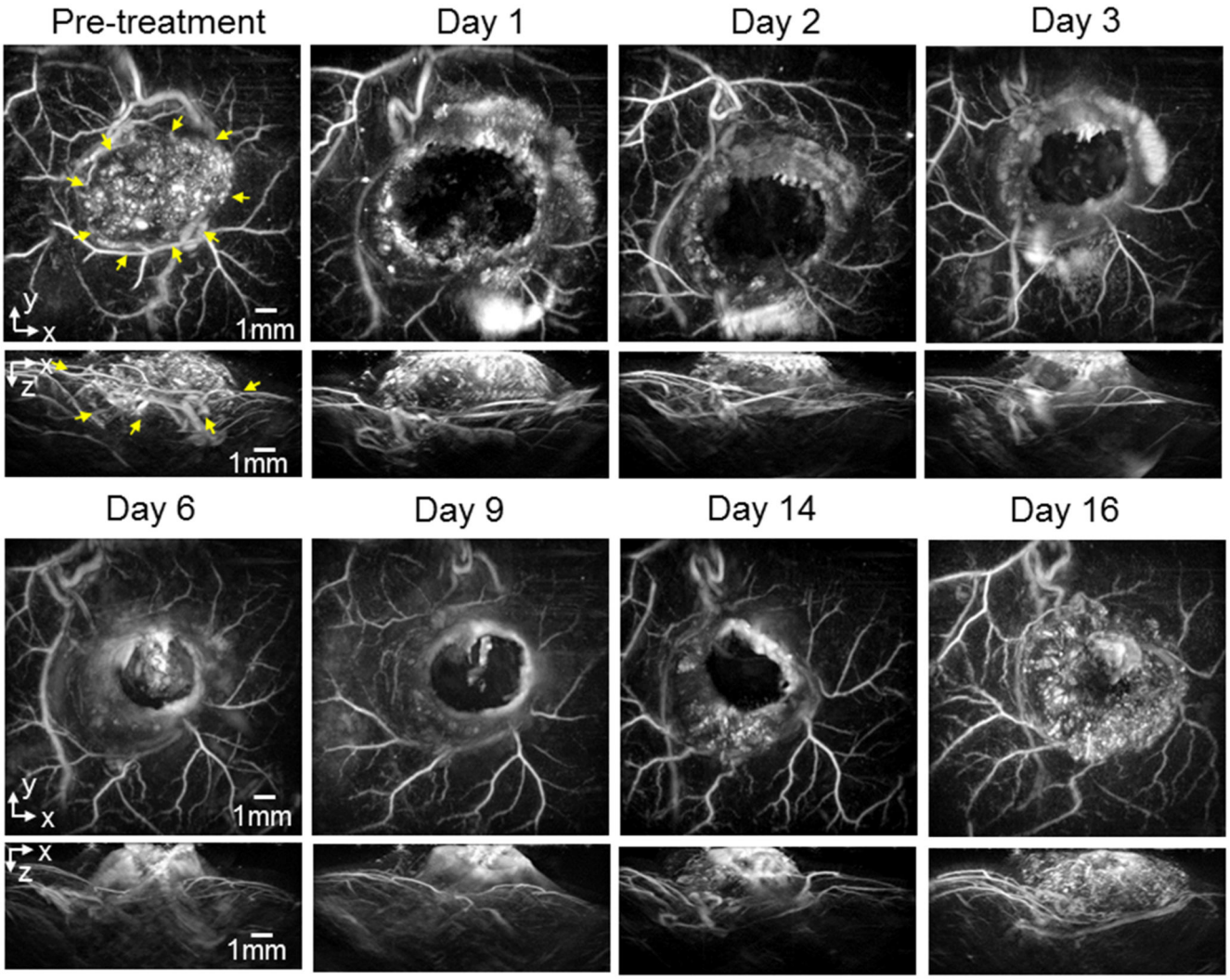

Figure 2.

Photoacoustic images displayed as maximum intensity projections (MIPs) showing the longitudinal response of a SW1222 tumor (mouse $m4_{sw}$) to 40mg/kg IV dose of OXi4503 over 16 days. The horizontal x-y maximum intensity projections (MIP) are for z = 1 - 6 mm. The tumour region in the pre-treatment image is indicated by yellow arrows. After treatment a region in the tumor core characterised by a lack of PAI contrast can be seen. This void diminishes over the 16 time course, with PA signal returning to areas of the tumor core.

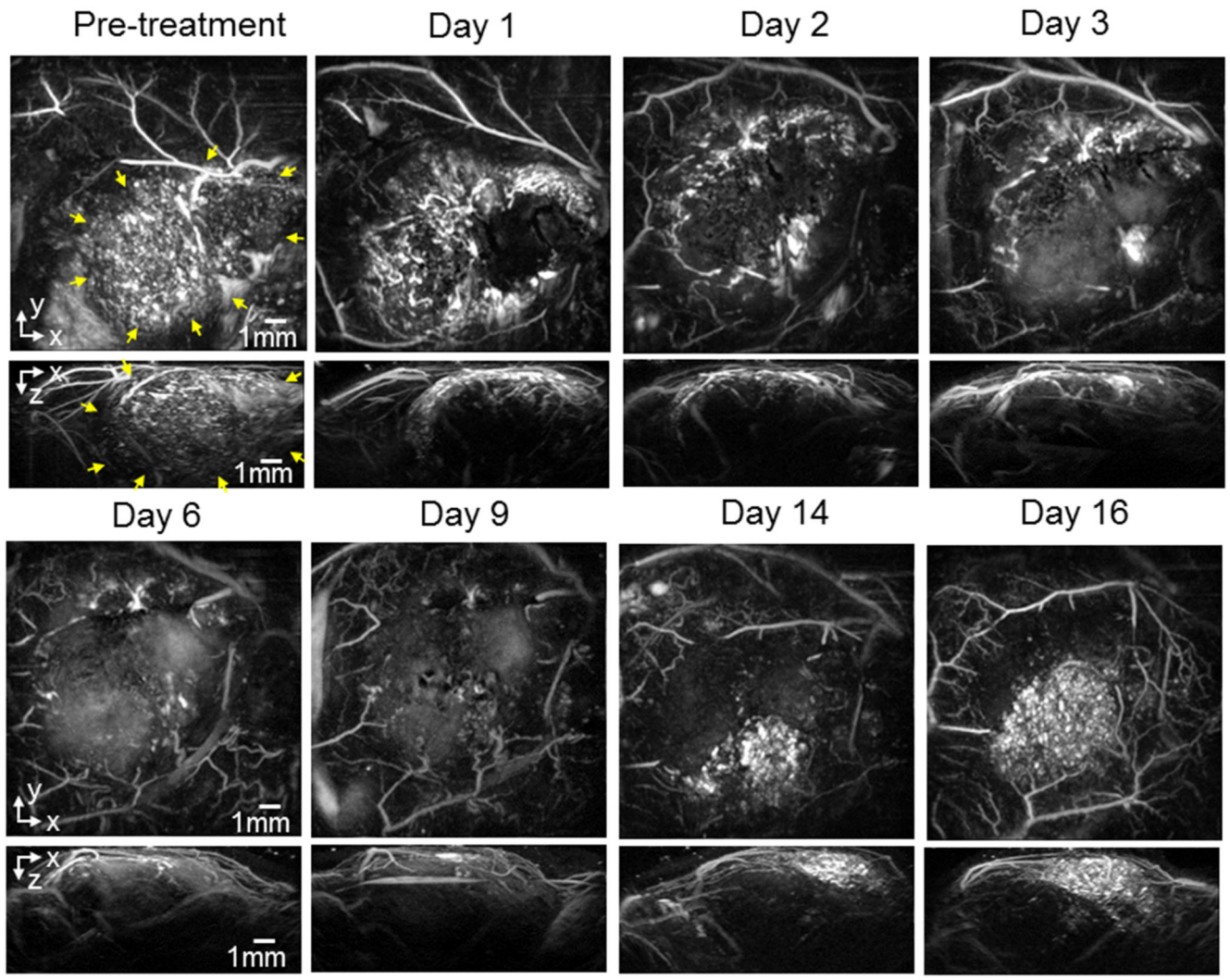

Figure 3.

Photoacoustic images displayed as maximum intensity projections (MIPs) showing the longitudinal response of a second subcutaneous SW1222 tumor (mouse $m3_{sw}$) to 40mg/kg IV dose of OXi4503 over 16 days. The horizontal x-y MIPs are for z = 1 - 6 mm. The pre-treatment vertical x-z MIP shows the tumor (indicated with yellow arrows) growth into the body of the mouse, rather than protruding outwards as seen in the previous example of figure 2. After treatment, the destruction and regrowth of the fine vascular signal in the tumor core can therefore be observed clearly in not only the horizontal MIPs, but also in the vertical MIPs.

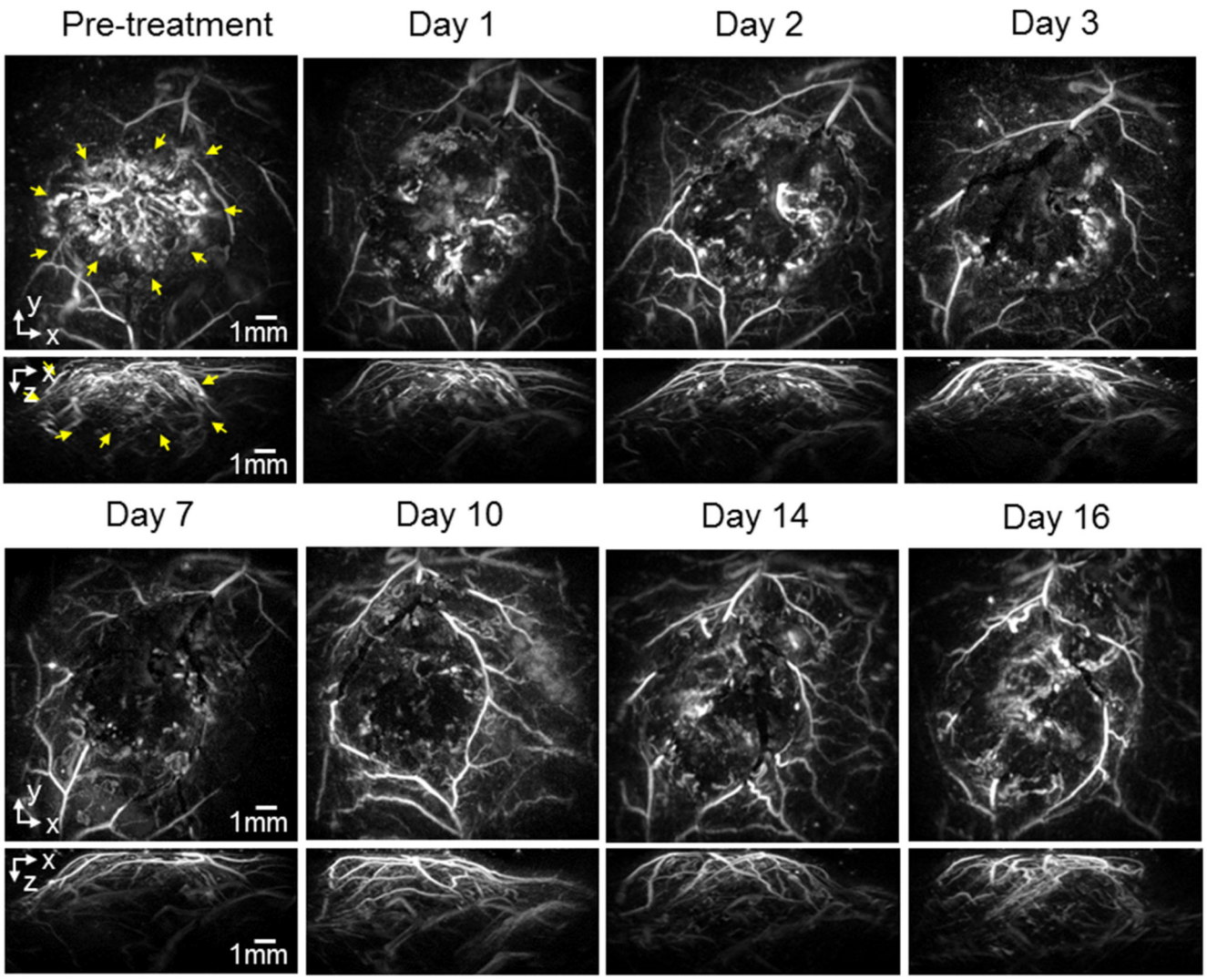

Figure 4.

Photoacoustic images displayed as maximum intensity projections (MIPs) showing the longitudinal response of an LS174T tumor (mouse $m4_{LS}$) to 40mg/kg IV dose of OXi4503 over 16 days. The horizontal x-y MIPs are for z = 1-6 mm. The vessel network in the tumor region, indicated with yellow arrows in the pre-treatment images, is seen to consist of relatively large sparsely distributed vessels, when compared to the spatially averaged vascular PA signal seen in the more highly vascularised homogenous SW1222 tumors. After treatment, a region in the tumor core which is characterised by a lack of contrast can be seen, due to the disruption of vessels.

Europe PMC Funders Author Manuscripts

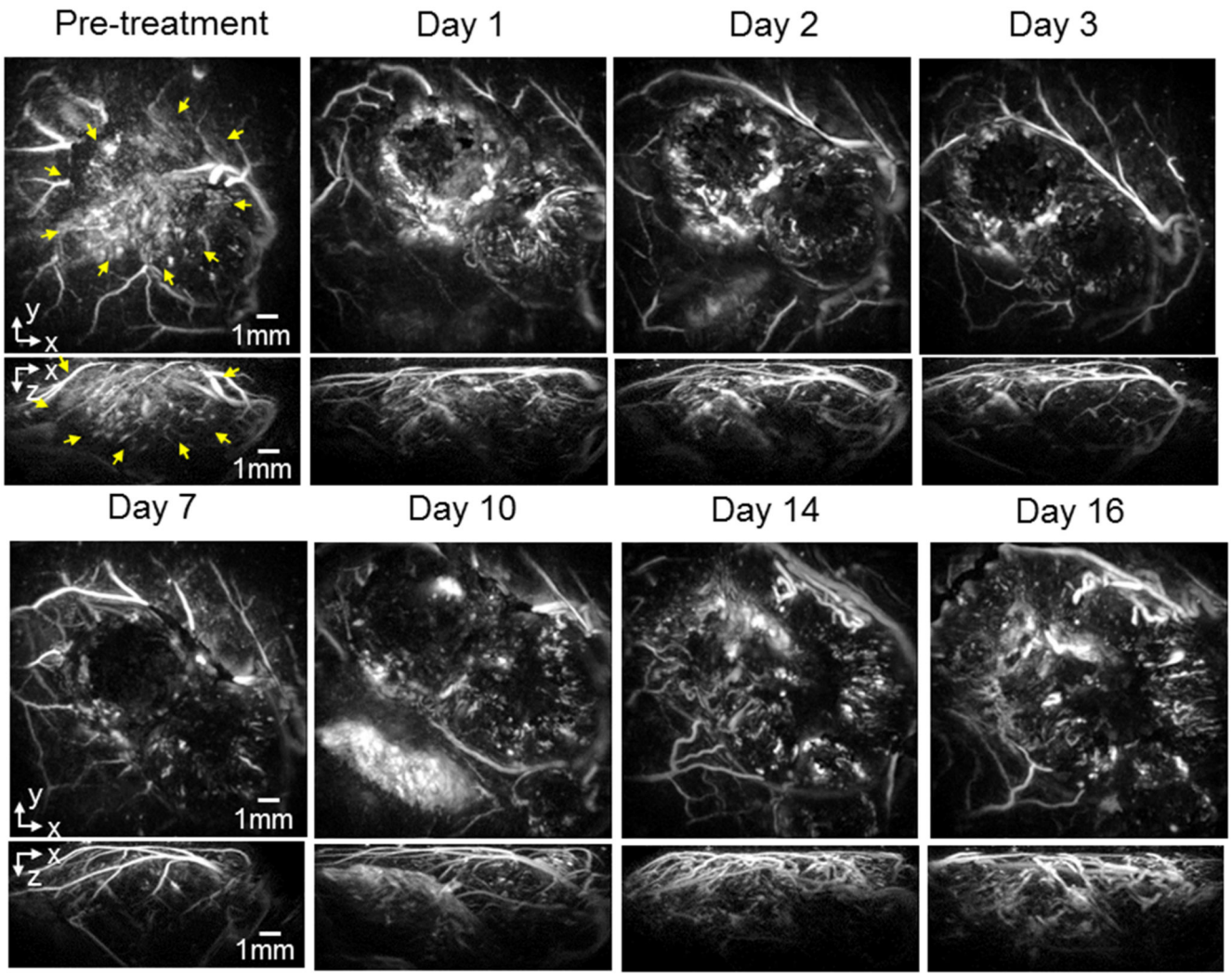

Figure 5.

Photoacoustic images displayed as maximum intensity projections (MIPs) showing the longitudinal response of a second LS174T tumor (mouse $m2_{LS}$) to 40mg/kg IV dose of OXi4503 over 16 days. The horizontal x-y maximum intensity projections (MIP) are for z = 1 - 6 mm. After treatment, the loss of signal contrast in the tumor region (indicated with yellow arrows in the pre-treatment images) is still significant even at Day 16

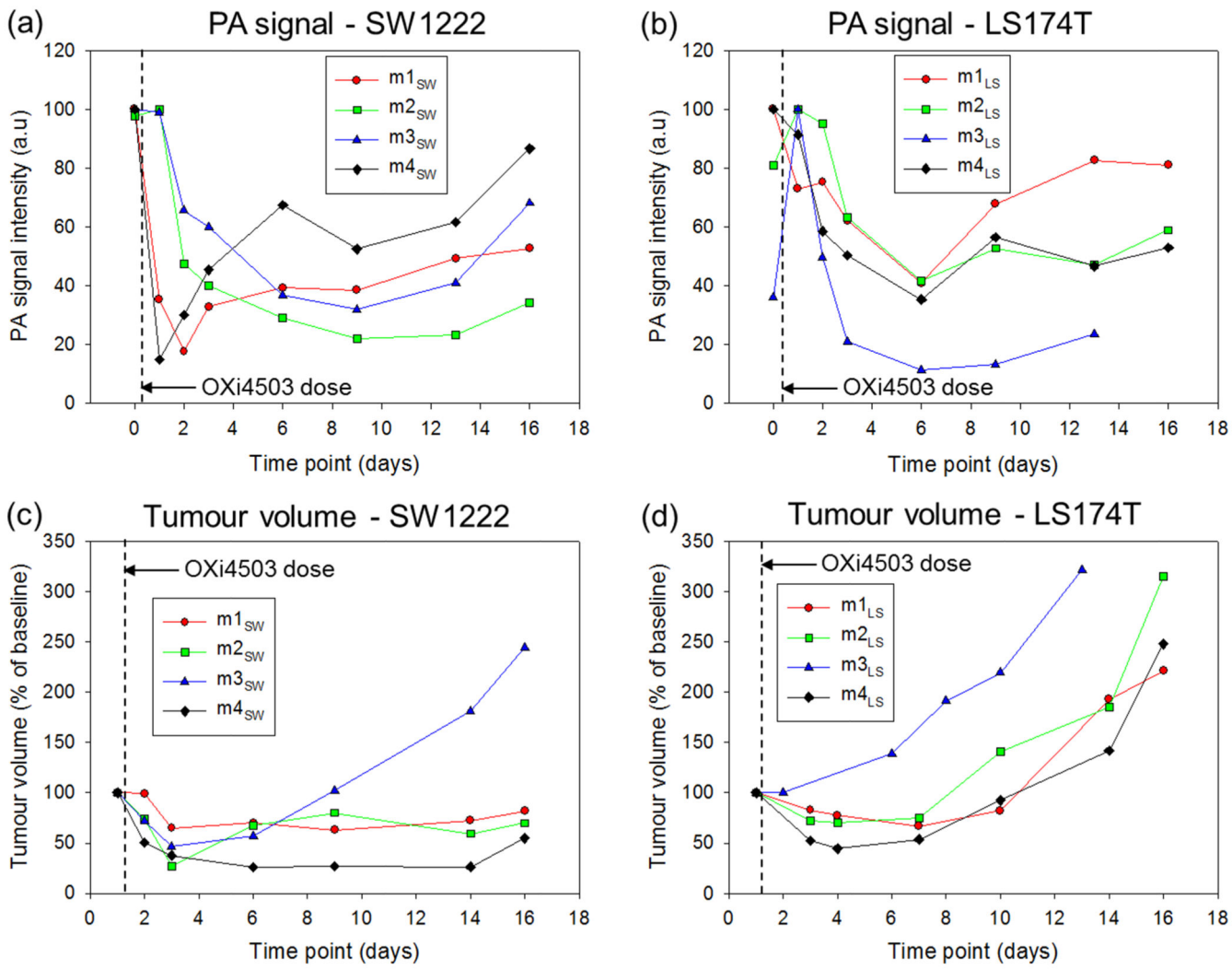

Figure 6.

Photoacoustic (PA) signal intensity and tumor volume of the two tumor types treated with 40mg/kg of OXi4503. Photoacoustic signal at different time points for (a) SW1222 and (b) LS174T tumors. Tumor volume measured by callipers at corresponding time points for (c) SW1222 and (d) LS174T tumors. For both tumor types, the PA signal intensity reduces after treatment before increasing again almost to pre-baseline levels. This is in agreement with the post-treatment destruction of the tumor core and subsequent repopulation of the vasculature, as shown in the PA images Figure 2–5. The tumor volumes in the SW1222 predominantly show an arrest in the tumor growth after treatment, up to day 16. In the LS174 tumors, an initial reduction in volume after treatment is followed by an increase at the later time points. SW1222: the PA signal data for mice $m4_{SW}$ and $m3_{SW}$ was obtained from the images shown in figures 2 and 3 respectively. LS174T: the PA signal data for mice $m4_{LS}$ and $m2_{LS}$ was obtained from the images shown in figures 4 and 5 respectively

Europe PMC Funders Author Manuscripts

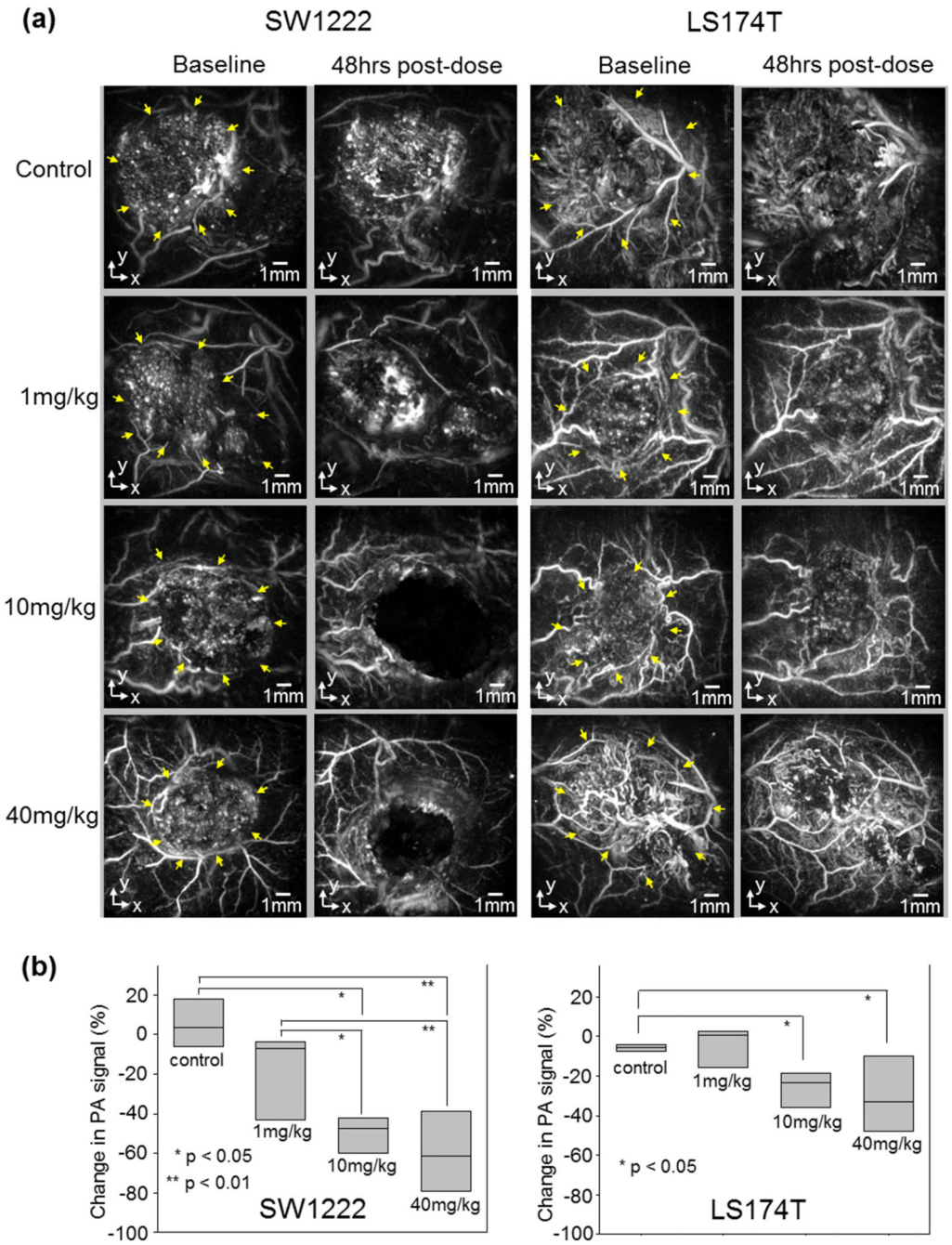

Figure 7.

(**a**) Sample of photoacoustic images (x-y MIPs) showing the response of two types of human colorectal tumor (SW1222, LS174T) to different dose of OXi4503. Yellow arrows in baseline images indicate the location of the tumor. The images are shown before IV treatment and 48 hours after treatment with saline, 1mg/kg, 10mg/kg or 40mg/kg. OXi4503 can be seen to produce a vascular disrupting response in the SW1222 down to 1mg/kg. The effect of OXi4503 on the LS174T tumors is reduced at 40mg/kg and 10mg/kg and negligible at 1mg/kg. (**b**) Percentage change in PA signal intensity of the two tumor types after

treatment for groups of n≥4 mice, except SW1222 control and LS174T 1mg/kg where n = 3. The treatment is seen to produce the greatest dose dependent response in the SW1222, compared to the LS174T. This is consistent with the extent of vascularisation being greater in the SW1222 tumors.

Europe PMC Funders Author Manuscripts